

Manuscript version: Published Version

The version presented in WRAP is the published version (Version of Record).

Persistent WRAP URL:

<http://wrap.warwick.ac.uk/173579>

How to cite:

The repository item page linked to above, will contain details on accessing citation guidance from the publisher.

Copyright and reuse:

The Warwick Research Archive Portal (WRAP) makes this work by researchers of the University of Warwick available open access under the following conditions.

Copyright © and all moral rights to the version of the paper presented here belong to the individual author(s) and/or other copyright owners. To the extent reasonable and practicable the material made available in WRAP has been checked for eligibility before being made available.

Copies of full items can be used for personal research or study, educational, or not-for-profit purposes without prior permission or charge. Provided that the authors, title and full bibliographic details are credited, a hyperlink and/or URL is given for the original metadata page and the content is not changed in any way.

Publisher's statement:

Please refer to the repository item page, publisher's statement section, for further information.

For more information, please contact the WRAP Team at: wrap@warwick.ac.uk

Active THz beam shaping using a one-dimensional array of photoconductive emitters

Cite as: Appl. Phys. Lett. **122**, 061102 (2023); doi: [10.1063/5.0132207](https://doi.org/10.1063/5.0132207)

Submitted: 27 October 2022 · Accepted: 18 January 2023 ·

Published Online: 6 February 2023



View Online



Export Citation



CrossMark

Nishtha Chopra,^{a)} Justas Deveikis,  and James Lloyd-Hughes^{a)} 

AFFILIATIONS

Department of Physics, University of Warwick, Gibbet Hill Road, Coventry CV4 7AL, United Kingdom

^{a)}Authors to whom correspondence should be addressed: Nishtha.Chopra@warwick.ac.uk and J.Lloyd-Hughes@warwick.ac.uk

ABSTRACT

The spatial profile of a beam of pulsed terahertz (THz) radiation is controlled electrically using a multi-pixel photoconductive emitter, which consists of an array of interdigitated electrodes fabricated on semi-insulating GaAs. Activating individual pixels allows the transverse position of the THz beam's focus to be varied off-axis, as verified by spatial beam profiles. Enabling multiple pixels simultaneously permits non-Gaussian beam shapes to be created. The diffraction-limited performance of the system is established by comparison with the Abbé and Sparrow criteria, and a condition for effective beam steering using this design is derived. The spatial resolution of the approach is linked to the frequency of the THz radiation and the f-number of the collection optic.

Published under an exclusive license by AIP Publishing. <https://doi.org/10.1063/5.0132207>

Terahertz technology is evolving rapidly, with a surge of new devices, materials, optics, and powerful data processing algorithms. At the center stage of many scientific and industrial developments lies terahertz time-domain spectroscopy (THz-TDS), which is facilitating an impact in nondestructive testing,^{1,2} medical diagnostics,³ and remote sensing.⁴ The technological development of improved, integrated THz systems may enable new applications, such as 6G communications and on-chip sensing.

The key to many future applications lies in improving the characterization and control of THz beams, bringing into the limelight the concepts of THz beam steering and beam shaping. In particular, applications such as medical imaging and communication may require efficient, compact modulators that can directly manipulate THz beams. For instance, temporal shaping and encoding of information on a THz beam are desired to achieve high data rates for communications,^{5,6} while active beam steering may also be desirable to aim effectively from a transmitter to a receiver. For THz imaging, understanding the beam's spatiotemporal profile can lead to an improved image resolution within the diffraction limit of the system.

Various methods that can alter the shape of a THz beam have been reported, including using 3D-printed phase waveplates,⁷ paper diffractive optics,⁸ metasurfaces,⁹ and THz spatial light modulators (SLMs) based on electrically modulated metasurfaces^{10,11} or optically patterned silicon.^{12,13} These technologies alter the amplitude and/or the phase of parts of a THz beam and have different degrees of tunability. However, the added complexity, extra system weight, and finite

insertion loss propel the need to develop integrated devices that can shape or steer a THz beam directly from the THz emitter.

Since the demonstration of the first photoconductive THz antennae (PCA), the technology has evolved with many design and material variations. The reliable performance and high dynamic range make PCA the THz source of choice in many commercial and scientific THz-TDS systems. Multi-pixel PCA were first demonstrated in 1991 by Froberg *et al.*, who used a PCA with 64 parallel electrodes excited at oblique incidence to produce a sequence of THz pulses, creating a time-division multiplexer.⁵ Arrays of dipole antennae have been used as photoconductive detectors of THz pulses, for example, a 16 pixel linear design with integrated microlenses¹⁴ or an 8×8 2D array combined with an optical SLM.¹⁵ Recently, multi-pixel PCA designs with interdigitated electrodes^{16,17} have been used to generate broadband THz pulses with high-purity linear,^{16,17} circular,¹⁸ radial, or azimuthal polarization.¹⁹

In this article, we report a linear array of interdigitated PCA designed and fabricated to electrically control the spatial beam profile, thus providing a compact and effective source for the on-demand control of a THz beam's position and shape. We measured the THz beam's profile under different electrical biasing schemes, allowing the THz beam's position to be varied and its shape to be altered away from a Gaussian profile. We demonstrate the diffraction-limited performance of the system and discuss how the finite size of the optics limits the spatial resolution achievable in the image plane by considering the propagation of different spatial frequencies through the spectrometer.

The multipixel emitter geometry, shown in Fig. 1, consisted of interdigitated electrodes with $5\ \mu\text{m}$ width and $20\ \mu\text{m}$ period. The electrodes were interwoven together and contacted such that every five pairs formed a $100\ \mu\text{m}$ -wide pixel. In contrast to the $\sim 20\ \mu\text{m}$ size of typical dipole PC antennae, which require Si lenses for beam collimation, the larger pixel width creates a less divergent beam that can be collected with the use of high numerical aperture optics, without a Si lens. The complete device consists of ten active pixels that were electrically controlled by varying the bias voltage amplitude. Arrays were fabricated on $500\ \mu\text{m}$ -thick undoped SI-GaAs using UV photolithography and metal

deposition with an e-beam evaporator. The substrate was spin-coated with a thin uniform layer of image reversal photoresist, and a chrome-plated mask was used to pattern the design onto the substrate by exposing UV light with a fluence of $90\ \text{mJ cm}^{-2}$. After development, the negative of the desired pattern was produced, with a clean under-cut. Topographically, interdigitated PCA devices can be divided into three layers:^{20–22} (a) a contact layer, with Ti/Au contacts $5\ \text{nm}/300\ \text{nm}$ thick; (b) an electrically insulating, $110\ \text{nm}$ -thick Al_2O_3 layer, which also acts as an anti-reflection coating for the $800\ \text{nm}$ excitation beam;²³ and (c) a shadow mask layer, which prevents regions with opposing electric field being photoexcited.²⁰ Bias voltages were applied to the multi-pixel PCA using a lab-built circuit based on an Arduino microcontroller, which allowed computer control of the voltage level applied to each pixel. In this work, a $100\ \text{kHz}$ square wave with 50% duty cycle and $10\ \text{V}$ amplitude was applied when pixels were turned on. Variable voltage levels allow further fine-tuning of beam profiles,¹⁹ but a fixed $10\ \text{V}$ maximum was used here.

A standard THz-TDS system with $3\ \text{THz}$ bandwidth and based on a $800\ \text{nm}$, $80\ \text{MHz}$, $100\ \text{fs}$ Ti:sapphire laser oscillator, was used to characterize the emission properties of the linear array PCA, as pictured in Fig. 1(b). Of note are the emitter plane, in which the voltages applied to each pixel defined the THz beam profile produced; the imaging plane, where the focused THz beam was profiled; and the detection plane, where the THz beam was re-imaged and detected. In the emitter plane ($x' - y'$), the 1D array was oriented in the x' -direction, perpendicular to the beam propagation axis. To excite the pixels more uniformly, the pump beam was expanded along x' by a plano-convex cylindrical lens ($f = 300\ \text{mm}$), forming a Gaussian profile with standard deviation $\sigma_{x'} = 830\ \mu\text{m}$. The pump's profile extended past the device's edges, and hence the transient photocurrent $J(x', t)$ [Fig. 1(c)] and THz field $E \propto \partial J / \partial t$ emitted²³ varied from pixel to pixel. The beam was focused in y' to $\sigma_{y'} = 98\ \mu\text{m}$. A fluence of $7.8\ \mu\text{J cm}^{-2}$, calculated using the elliptical beam's area, excited the PCA array. The array was at the focus of the first off-axis parabolic mirror (OAP), which had a diameter $D = 50.8\ \text{mm}$ and an effective focal length $f_1 = 50.8\ \text{mm}$. The probe beam ($< 1\ \text{mW}$ power) sampled the THz beam in the detection plane ($x'' - y''$) using a (111)-oriented GaP electro-optic crystal.²⁴ An elliptical probe beam spot with a width $\sigma_{x''} = 0.9\ \text{mm}$ and a height $\sigma_{y''} = 89\ \mu\text{m}$ ensured that the horizontal extent of the probe beam matched the position of the THz beams from each pixel [Fig. 1(d)]. Alignment was first obtained by overlapping the scattered pump beam from the emitter position with the probe beam using an imaging CCD camera at the detection position. The PCA array was then aligned in the pump beam based on the THz electro-optic signal with pixel 5 active, before adjusting the probe beam position. The electro-optic signal, $\Delta I(t) = AIE(t)$, was proportional to the THz electric field strength $E(t)$, total probe signal I , and the constant $A = (\sqrt{24/3})(2\pi/\lambda)r_{41}n^3L = 4.2 \times 10^{-8}\ \text{mV}^{-1}$, which depends on the probe beam's wavelength, $\lambda = 800\ \text{nm}$, and the electro-optic coefficient $r_{41} = 0.5\ \text{pm V}^{-1}$, refractive index $n = 3.2$, and thickness $L = 200\ \mu\text{m}$ of the GaP electro-optic crystal.²⁵

$\Delta I/I$ was recorded as a function of pump-probe time delay t for a variety of different electrical biasing conditions applied to the PCA. The maximum $\Delta I/I = 8.3 \times 10^{-5}$ corresponded to a peak THz electric field $E = 2\ \text{kV m}^{-1}$ with all pixels active. Furthermore, in order to determine the THz beam's profile, a razor blade was scanned horizontally in the imaging plane, along x , while recording the electro-optic

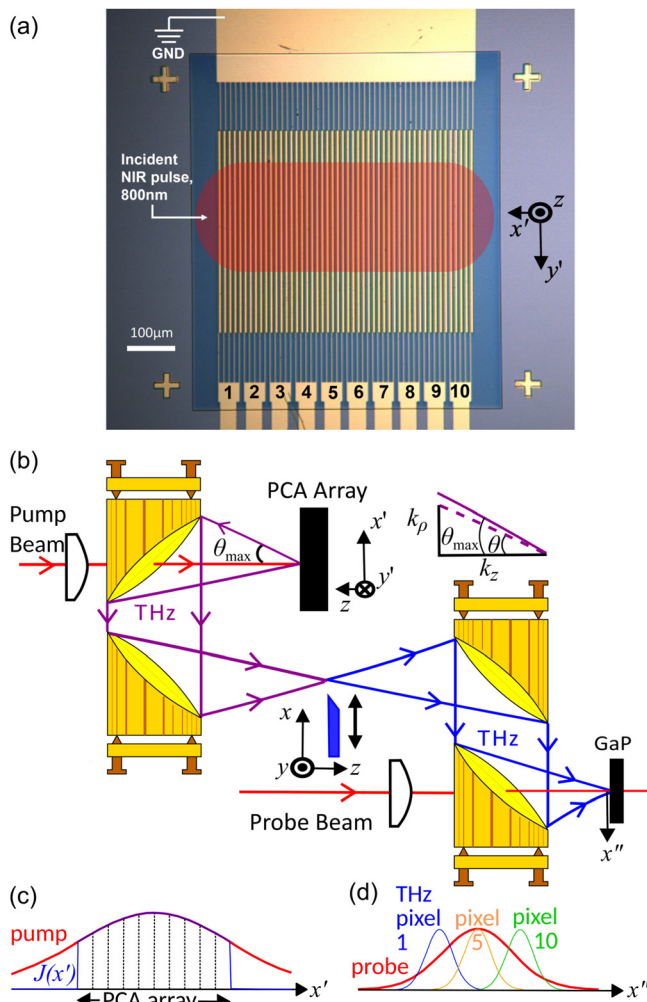


FIG. 1. (a) Micrograph of linear PCA array with interdigitated stripline electrodes fabricated on SI-GaAs, with ten individually biased electrodes. (b) Schematic of experimental geometry showing the emitter beam path. In the $x-y$ imaging plane, the knife edge (blue) profiled the THz beam along x . Cylindrical lenses produced the appropriate beam profile horizontally for the pump and probe beams. Inset, top-right: a plane wave at angle θ to the z -axis has transverse and longitudinal wavevectors, k_p and k_z , respectively, and propagates through the system if $\theta < \theta_{\text{max}}$. (c) Schematic profiles of pump beam (red) and photocurrent $J(x')$ (blue) at the emitter, along the x' -direction. (d) Profiles of probe beam (red) and THz beams from selected individual pixels (blue, orange, and green).

signal. The electric field profile at the peak of the THz pulse was obtained by numerically differentiating the electro-optic signal, utilizing $E(x, t = 0) \propto \frac{\partial}{\partial x} \Delta I(x, t = 0)$. Profiles were obtained at different positions along the beam propagation axis, z , in order to find the focus ($z = 0$). Where applicable, we used a Gaussian fit to the electric field profile, $E(x)$.

When the linear array was operated in a pixel sweeping mode, each pixel was individually switched on, with a peak bias of 10 V, while all other pixels were grounded. The electric field pulses recorded in the time domain, $E(t)$, are shown in Fig. 2(a) for pixels 1, 5, and 10. The normalized THz pulses produced by each pixel have similar time-domain shape and spectral content, with a small shift in phase (< 0.1 ps) associated with the small differences in optical path lengths for pixels 1 and 10, centered at $x' = \pm 450 \mu\text{m}$ relative to the center of the device at $x' = 0$. In Fig. 2(b), the transverse profiles of the peak THz electric field, $E(x, t = 0)$, in the imaging plane, are reported for each individual pixel. A Gaussian electric field profile was seen for each pixel, with a similar width $\sigma_x = 0.25 \text{ mm}$, but with a beam center that varied linearly with the pixel number [Fig. 2(c)]. This demonstrates that the multi-pixel PCA 1D array can be used to obtain line-scan THz images at different transverse positions in the imaging plane, without having to raster scan a sample. Note that the maximum transverse shift in beam center obtained between pixels 1 and 10 (1.3 mm) was larger than the spacing between their centers (0.9 mm) as a result of the finite magnification $M = f_2/f_1 = 1.5$ of the image formed by the second OAP, which had a longer focal length ($f_2 = 76.2 \text{ mm}$) than the first OAP ($f_1 = 50.8 \text{ mm}$). The similar beam profile and beam width for each pixel imply that there were no substantial aberrations or alignment issues with the reported spectrometer. The transverse shift is $\Delta x = M\Delta n d$ for two pixels with a difference in pixel number Δn and pixel period $d = 100 \mu\text{m}$.

To demonstrate that the beams from each pixel combined constructively in the far field, Fig. 3(a) reports beam profiles obtained for

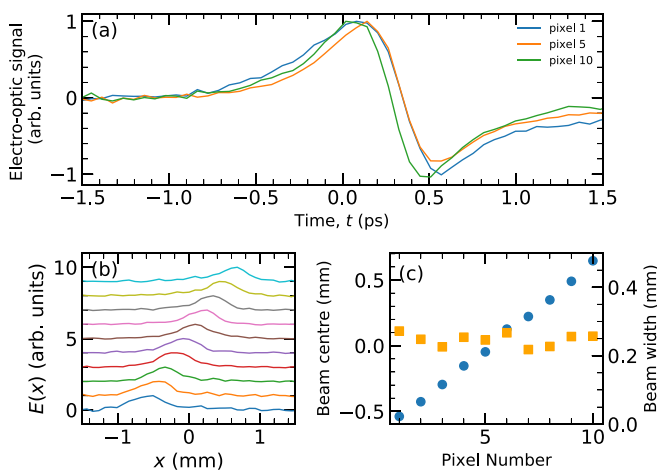


FIG. 2. (a) Normalized THz time-domain waveforms with only pixels 1, 5, or 10 active. (b) Beam profiles at the sample focus in pixel sweeping mode, with one pixel on at a time. From bottom to top: pixels 1 to 10. Data are normalized and offset for clarity. (c) Beam centers (blue circles, left axis) and beam widths (orange squares, right) for each pixel, extracted from Gaussian fits to the profiles in (b). The beam center shifted linearly with pixel number, while the beam width was the same for each pixel, with $\sigma_x = 0.25 \text{ mm}$.

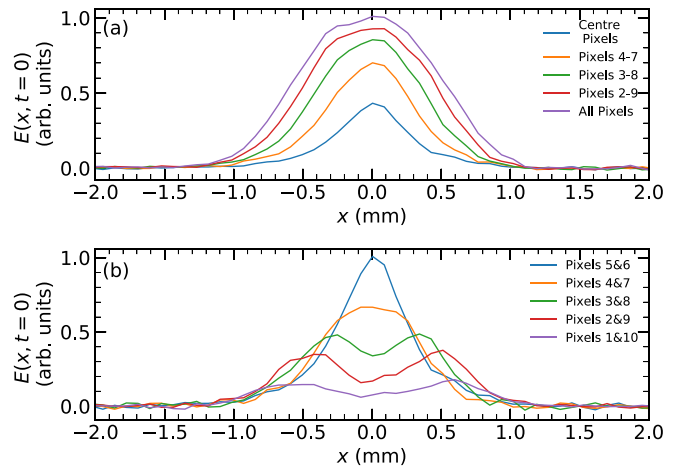


FIG. 3. (a) Beam profiles $E(x, t = 0)$ from knife edge measurements when pixels were switched on simultaneously starting from the central two pixels (5 and 6, blue line, $n = 2$) to all pixels (1 to 10, purple line, $n = 10$). Data were scaled relative to the case where all pixels were on. (b) THz beam profiles for two pixels on, with a varying gap of dark pixels between them.

cases with a different number of pixels, n , switched on symmetrically about the axis, from pixels 5 and 6 ($n = 2$, blue line) to all pixels ($n = 10$, purple line). When more pixels were turned on the amplitude grew and the beam broadened in width. With all pixels active, the measured $E(t)$ was the same as the sum of the THz waveforms for each pixel on individually, demonstrating that there was no noticeable destructive interference. Theoretically, with n pixels active the beam profile should be the convolution of a top-hat (width Mnd) and a Gaussian (representing the diffraction-limited spot size). Initially, for $n = 2$ (pixels 5 and 6 on), the electric field had a Gaussian profile $\sigma_x = 0.28 \pm 0.01 \text{ mm}$, marginally larger than $\sigma_x = 0.25 \pm 0.01 \text{ mm}$ for pixel 5 alone, corresponding to a broadening due to diffraction larger than Mnd . With increasing n , the beam width (FWHM) grew linearly from 0.56 mm ($n = 2$) to 1.2 mm ($n = 10$). Note that the on-axis amplitude $E(x = 0)$ did not grow linearly with the number of active pixels, as the THz radiation from laterally offset pixels was focused away from the optical axis [Figs. 1(d) and 2(b)]. Furthermore, the 1.2 mm FWHM for $n = 10$ was smaller than the value expected from $Mnd = 1.5 \text{ mm}$, as the electro-optic signal from pixels away from the axis was smaller. This can be understood by considering Fig. 1(d) along with the expression for the electro-optic signal at a particular position, $\delta I(x'') = AE(x'')I(x'')$, where $E(x'')$ and $I(x'')$ are the THz beam's and probe beam's profiles. The total electro-optic signal measured was $\Delta I = \int \delta I(x'')dx'' = A \int E(x'')I(x'')dx''$, and hence for THz pulses from pixels further from the optical axis [e.g., pixels 1 and 10, Fig. 1(d)] the lower probe intensity created smaller electro-optic signal than for central pixels (e.g., pixel 5). Nonetheless, Fig. 3 demonstrates that the THz beam's width and amplitude were controllable by switching multiple pixels on or off.

To investigate the spatial resolution attainable with this multi-pixel design, we applied a bias voltage to two pixels, with an increasing number of “dark” pixels in-between the active pixels. Referring to Fig. 3(b), with pixels 5 and 6 active, the beam had a Gaussian profile, while for pixels 4 and 7 ($300 \mu\text{m}$ between pixel centers) the beam contained

a flatter central region. As the separation between pixel centers was increased further, from 500 μm (pixels 3 and 8 on) to 900 μm (pixels 1 and 10), the individual Gaussian profiles from each pixel became increasingly evident. This shows that with multiple pixels on, the multi-pixel PCA can produce arbitrary THz beam profiles in the imaging plane. We note that the electro-optic signal for pixel pairs further from the optical axis (e.g., 1 and 10; 2 and 9) was reduced as a result of the lower photocurrent [Fig. 1(c)] and lower probe intensity [Fig. 1(d)].

To establish the performance of this approach, we compared our results with diffraction theory. The minimum resolvable transverse spatial resolution, r , can be estimated for a diffraction-limited beam using either the Sparrow criterion, $r = 0.47\lambda/\text{NA}$, or the Abbé criterion, $r = \lambda/2\text{NA}$, where the numerical aperture $\text{NA} = D/(2f_1) = 0.33$ for the focusing OAP. At 1 THz, the center frequency of the THz pulses, this yields $r = 427$ and $r = 450 \mu\text{m}$ for the Sparrow and Abbé cases, respectively. The Sparrow criterion yields a flat-top profile, as seen for the case where pixels 4 and 7 are on [Fig. 3(b)], and the width of the flat top corresponds to r . The experimental width of the flat top was $\sim 440 \mu\text{m}$, in good agreement with the theory.

Having established that the setup had diffraction-limited performance, we now establish a criterion for when beam steering is possible for a given design and wavelength. The shift in beam center should be larger than r , otherwise the beam shift may not be resolvable, hence $\Delta x = M\Delta nd > r$. Taking the Abbé value for r yields $(f_2/f_1)\Delta nd > \lambda f_2/D$ or $\Delta nd > \lambda$, since $f_1 = D$ in this setup. Hence, beam steering can be obtained when pixels are separated by $\Delta nd > \lambda$, requiring $\Delta n > 3$ at 1 THz. At higher frequencies (shorter wavelengths), the smaller diffraction-limited beam size makes it easier to steer the beam.

We now consider the propagation of THz radiation through our optical setup in order to discuss another factor affecting image resolution in the imaging plane. The propagation of light away from an extended source can be considered by decomposing the beam into a sum of plane waves, each traveling at an angle θ to the propagation axis [inset in Fig. 1(b)], where $\tan \theta = k_\rho/k_z$ for transverse wavevector k_ρ , axial wavevector k_z , and wavevector k . The maximum angle, θ_{max} that a wave from a point in the emitter plane (near the optical axis) can have while still being collected by the first optic is given by $\tan \theta_{\text{max}} = D/2f_1$. From the condition $\tan \theta \leq \tan \theta_{\text{max}}$ for waves to propagate through the optical system, we find $k_\rho/k_z \leq D/2f_1$, leading to the condition that waves traveling to the imaging plane have a sufficiently small transverse wavevector k_ρ , given by

$$k_\rho \leq k_{\rho,\text{max}} = \frac{D}{2f_1} \frac{1}{\sqrt{1 + D^2/4f_1^2}} \frac{\omega}{c}. \quad (1)$$

The image of the emitter formed in the image plane is, therefore, missing the plane waves with higher transverse wavevectors, $k_\rho > k_{\rho,\text{max}}$. When the higher transverse wavevectors (higher spatial frequencies) are lost, the fine detail in the image is blurred out. The highest spatial frequency in the image, $\nu_{\text{max}} = k_{\rho,\text{max}}/2\pi$, determines the spatial resolution, Δx via

$$\Delta x \simeq 1/\nu_{\text{max}} = 2\pi/k_{\rho,\text{max}}. \quad (2)$$

Note that Δx and $k_{\rho,\text{max}}$ depend solely on the THz radiation's frequency (or wavelength) and the collection optic's f-number f_1/D .

To explore the frequency-dependent resolution of our system, THz time-domain waveforms were acquired for different knife edge positions along x , with all pixels active. The amplitude spectrum of the

electro-optic signal, $|\Delta I(x, \omega)|$, is reported in Fig. 4(a). The electric field profile at different frequencies was obtained from $|E(x, \omega)| \propto \partial|\Delta I|/\partial x$ and is reported in Fig. 4(b), which corresponds to a cross-sectional image of the pattern produced by the emitter array. At 100 GHz, the beam profile was Gaussian and broad, while at 1 THz it was narrower, and at 1.8 THz and higher, the profile had a sharper, more top-hat-like shape. Considering Eq. (1) shows that for lower THz frequencies (smaller ω) the spatial cut-off frequency ν_{max} is reduced, and hence the image is more substantially blurred, allowing an intuitive understanding of the results in Fig. 4. Quantitatively, at $\omega/2\pi = 1$ THz, we find $\Delta x \simeq 0.6$ mm using Eqs. (1) and (2), while at 2 THz $\Delta x \simeq 0.3$ mm, in good agreement with the minimum feature size (the width of the step) seen in Fig. 4(b).

Here, we demonstrated a versatile approach to dynamically steer and shape THz beams, based on multi-pixel PCA technology. In this prototype, the beam profiles and image resolution were measured and assessed with different combinations of the ten pixels active. Each pixel produced the same bandwidth THz pulse but at different transverse positions in the imaging plane. Tuning the voltage applied to each pixel allowed the amplitude and profile of the generated THz beam to be modified, without changing its phase. The concept is readily extendable to larger pixel numbers and to 2D emitter arrays, which will allow the rapid modulation of the THz beam's position across different locations on a sample. In this design, while the PCA arrays can be driven at high frequency (e.g., 100 kHz here, limited by the lock-in amplifier's bandwidth), the maximum pixel sweeping rate is lower: it cannot exceed the detection rate, in this case set by the lock-in

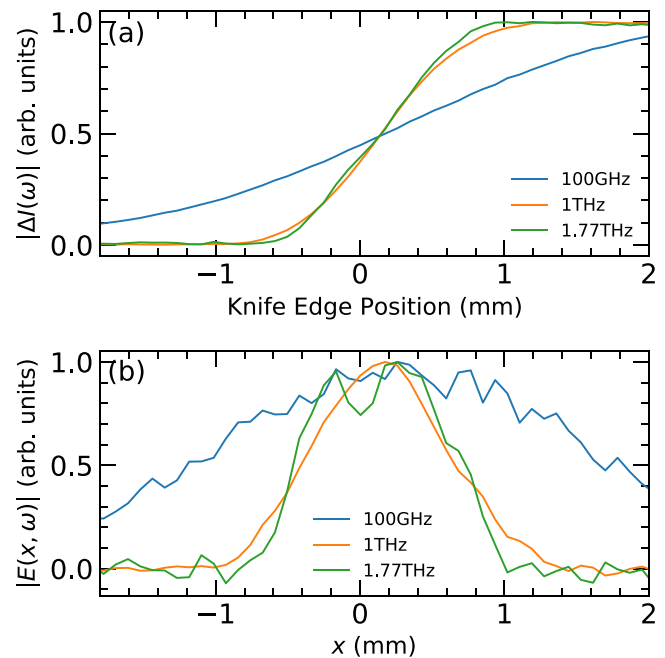


FIG. 4. (a) The frequency-resolved amplitude of the electro-optic signal vs knife-edge position, normalized. (b) Numerical spatial differentiation of the data in (a) yields the spatial profile of the THz beam at different frequencies: lower frequencies are substantially blurred due to the finite spatial cut-off frequency of the spectrometer's collection optic [Eq. (1)].

amplifier's time constant (1 ms, or 1 kHz frequency). However, this may still allow real-time image acquisition via compressed sensing, but without the extra components required in current THz SLM systems, such as the extra laser, optical SLM, and semiconductor required for optically excited THz SLMs.^{12,13} Electrical modulator arrays based on metasurfaces¹¹ can change the amplitude or phase of a THz beam, in contrast to the current approach (amplitude only). THz SLMs have a finite modulation amplitude and operate over a restricted frequency range: for metasurface-based modulators, the modulation depth can be high only at the design frequency (near resonance), while optically pumped modulators have a bandwidth defined by the frequency-dependent conductivity of the semiconductor used and a modulation depth that depends on the semiconductor's carrier lifetime and mobility.^{13,26} In contrast, the PCA array approach has a high modulation amplitude (100%), is broadband (it covers the entire bandwidth of the THz pulse), and can perform full polarization control of linear, circular, and cylindrical vector beams.^{18,19}

The authors would like to acknowledge funding from the EPSRC (UK) (Grant No. EP/V047914/1).

AUTHOR DECLARATIONS

Conflict of Interest

The authors have no conflicts to disclose.

Author Contributions

Nishtha Chopra: Conceptualization (equal); Data curation (equal); Formal analysis (equal); Investigation (equal); Methodology (equal); Project administration (equal); Validation (equal); Visualization (equal); Writing – original draft (equal); Writing – review & editing (equal). **Justas Deveikis:** Investigation (supporting); Methodology (supporting); Resources (supporting); Writing – review & editing (supporting). **James Lloyd-Hughes:** Conceptualization (equal); Formal analysis (equal); Funding acquisition (equal); Project administration (equal); Resources (equal); Software (equal); Supervision (equal); Validation (equal); Visualization (equal); Writing – review & editing (equal).

DATA AVAILABILITY

The data that support the findings of this study are available from the corresponding author upon reasonable request.

REFERENCES

- ¹S. Zhong, *Front. Mech. Eng.* **14**, 273 (2019).
- ²S. D. Siv Sachin, V. Vijayan, and R. N. Kini, *J. Opt.* **24**, 044014 (2022).
- ³X. Chen, H. Lindley-Hatcher, R. I. Stantchev, J. Wang, K. Li, A. H. Serrano, Z. D. Taylor, E. Castro-Camus, and E. Pickwell-MacPherson, *Chem. Phys. Rev.* **3**, 011311 (2022).
- ⁴X. Fu, Y. Liu, Q. Chen, Y. Fu, and T. J. Cui, *Front. Phys.* **10**, 869537 (2022).
- ⁵N. M. Froberg, B. B. Hu, X. C. Zhang, and D. H. Auston, *Appl. Phys. Lett.* **59**, 3207 (1991).
- ⁶L. Gingras and D. G. Cooke, *Optica* **4**, 1416 (2017).
- ⁷J. Gospodarcic, A. Kuzmenko, A. Pimenov, C. Huber, D. Suess, S. Rotter, and A. Pimenov, *Appl. Phys. Lett.* **112**, 221104 (2018).
- ⁸A. Siemion, J. Suszek, A. Kowalczyk, J. Bomba, A. Sobczyk, N. Palka, P. Zagrajek, A. Kolodziejczyk, and M. Sypek, *IEEE Trans. Terahertz Sci. Technol.* **6**, 568 (2016).
- ⁹X. Li, Z. Shen, Q. Tan, and W. Hu, *Front. Phys.* **9**, 659747 (2021).
- ¹⁰W. L. Chan, H. T. Chen, A. J. Taylor, I. Brener, M. J. Cich, and D. M. Mittleman, *Appl. Phys. Lett.* **94**, 213511 (2009).
- ¹¹C. M. Watts, D. Shrekenhamer, J. Montoya, G. Lipworth, J. Hunt, T. Sleasman, S. Krishna, D. R. Smith, and W. J. Padilla, *Nat. Photonics* **8**, 605 (2014).
- ¹²R. I. Stantchev, B. Sun, S. M. Hornett, P. A. Hobson, G. M. Gibson, M. J. Padgett, and E. Hendry, *Sci. Adv.* **2**, e1600190 (2016).
- ¹³I. R. Hooper, N. E. Grant, L. E. Barr, S. M. Hornett, J. D. Murphy, and E. Hendry, *Sci. Rep.* **9**, 18304 (2019).
- ¹⁴B. Pradarutti, R. Müller, W. Freese, G. Matthäus, S. Riehemann, G. Notni, S. Nolte, and A. Tünnermann, *Opt. Express* **16**, 18443 (2008).
- ¹⁵R. Henri, K. Nallappan, D. S. Ponomarev, H. Guerboukha, D. V. Lavrukhin, A. E. Yachmenev, R. A. Khabibullin, and M. Skorobogatiy, *IEEE Access* **9**, 117691 (2021).
- ¹⁶C. D. Mosley, M. Staniforth, A. I. Serrano, E. Pickwell-Macpherson, and J. Lloyd-Hughes, *AIP Adv.* **9**, 045323 (2019).
- ¹⁷K. Maussang, J. Palomo, J. Mangeney, S. S. Dhillon, and J. Tignon, *Opt. Express* **27**, 14784 (2019).
- ¹⁸C. D. Mosley, J. Deveikis, and J. Lloyd-Hughes, *Appl. Phys. Lett.* **119**, 121105 (2021).
- ¹⁹J. Deveikis and J. Lloyd-Hughes, *Opt. Express* **30**, 43293 (2022).
- ²⁰A. Dreyhaupt, S. Winnerl, T. Dekorsy, and M. Helm, *Appl. Phys. Lett.* **86**, 121114 (2005).
- ²¹C. D. Mosley, M. Failla, D. Prabhakaran, and J. Lloyd-Hughes, *Sci. Rep.* **7**, 12337 (2017).
- ²²A. Singh, H. Schneider, M. Welsch, M. Helm, and S. Winnerl, *Opt. Express* **27**, 13108 (2019).
- ²³C. Headley, L. Fu, P. Parkinson, X. Xu, J. Lloyd-Hughes, C. Jagadish, and M. B. Johnston, *IEEE J. Sel. Top. Quantum Electron.* **17**, 17 (2011).
- ²⁴N. C. J. van der Valk, W. A. M. van der Marel, and P. C. M. Planken, *Opt. Lett.* **30**, 2802 (2005).
- ²⁵N. C. J. van der Valk, T. Wenckebach, and P. C. M. Planken, *J. Opt. Soc. Am. B* **21**, 622 (2004).
- ²⁶M. G. Burdanova, G. M. Katyba, R. Kashtiban, G. A. Komandin, E. Butler-Caddle, M. Staniforth, A. A. Mkrtchyan, D. V. Krasnikov, Y. G. Gladush, J. Sloan, A. G. Nasibulin, and J. Lloyd-Hughes, *Carbon* **173**, 245 (2021).